

pubs.acs.org/JACS Article

Diffuse Ions Coordinate Dynamics in a Ribonucleoprotein Assembly

Ailun Wang, Mariana Levi, Udayan Mohanty,* and Paul C. Whitford*



Cite This: J. Am. Chem. Soc. 2022, 144, 9510-9522



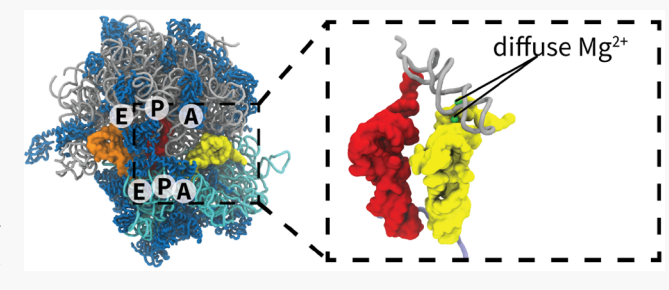
ACCESS I

Metrics & More

Article Recommendations

Supporting Information

ABSTRACT: Proper ionic concentrations are required for the functional dynamics of RNA and ribonucleoprotein (RNP) assemblies. While experimental and computational techniques have provided many insights into the properties of chelated ions, less is known about the energetic contributions of diffuse ions to large-scale conformational rearrangements. To address this, we present a model that is designed to quantify the influence of diffuse monovalent and divalent ions on the dynamics of biomolecular assemblies. This model employs all-atom (non-H) resolution and explicit ions, where effective potentials account for hydration



effects. We first show that the model accurately predicts the number of excess Mg^{2+} ions for prototypical RNA systems, at a level comparable to modern coarse-grained models. We then apply the model to a complete ribosome and show how the balance between diffuse Mg^{2+} and K^+ ions can control the dynamics of tRNA molecules during translation. The model predicts differential effects of diffuse ions on the free-energy barrier associated with tRNA entry and the energy of tRNA binding to the ribosome. Together, this analysis reveals the direct impact of diffuse ions on the dynamics of an RNP assembly.

INTRODUCTION

Many large-scale biomolecular processes in the cell depend on the presence of monovalent and multivalent ions. The contribution of cations to structure and dynamics has been experimentally documented for a variety of systems, including RNA, ¹⁻⁶ DNA, ^{7,8} and ribonucleoprotein (RNP) assemblies. ^{9,10} A particularly well-characterized RNP assembly is the ribosome, for which specific counterion concentrations are needed for assembly ^{11,12} and conformational transitions between functional states. ^{13,14} In terms of biological function, *in vitro* studies have revealed how ions can even regulate the accuracy of protein synthesis by the ribosome. ^{15,16} While the broad influence of counterions is acknowledged, identifying the physical—chemical relationship between ions and the mechanical properties of large-scale RNP assemblies has remained elusive.

The solvent environment around RNA is generally described as containing chelated and diffuse ions. 3,4 Chelated (i.e., innershell) ions are partially dehydrated, which allows them to form strong direct contacts with RNA. 3,4,17 As a result, chelated ions can remain bound to RNA for millisecond—second time scales, $^{18-20}$ which exceeds the duration of many biomolecular processes. In contrast, diffuse (outer-shell) ions maintain a coordinated hydration shell (e.g., $({\rm MgH_2O})_6^{\,2+})$ and associate less strongly with RNA. Even though water molecules can exchange rapidly (microseconds), $^{21-23}$ each ion remains fully hydrated. Accordingly, the behavior of a diffuse ion is primarily determined by longer-range electrostatic interactions. Despite the transient and weak influence of individual diffuse ions, their collective effect can be significant. For example, tRNA structural stability increases with the concentration of monovalent cations,

which can be attributed to screening effects and ion-mediated interactions. ^{24,25} The diffuse ionic environment can also control tertiary structure formation in RNA, including ribozymes ²⁶ and the ribosome. ²⁷ A complicating factor when studying diffuse ions is that monovalent and divalent ions competitively associate with RNA. Due to this, a balance of entropic and enthalpic factors can lead to nontrivial relationships between ionic concentrations and biomolecular stability/dynamics.

The essential roles of ions in biology has motivated their study over a wide range of temporal and spatial scales. There are now many computational approaches available that include implicit-solvent and all-atom explicit-solvent representations, as well as coarse-grained models. Within the class of implicit-solvent models, there have been applications of nonlinear Poisson—Boltzmann theory, ^{28–30} counterions condensation models, ^{31–36} reference interaction site model, ^{37–39} and Debye—Hückel (DH) treatments, ^{40–42} among other strategies. ^{43–45} While these methods can provide accurate representations of the local electric fields, it is common for these approaches to neglect ion—ion correlations, which can make it difficult to distinguish between the effects of monovalent and divalent species. ^{46,47} In the study of biomolecular assemblies, coarse-grained models frequently employ a DH treatment for monovalent ions. ⁴⁸ This

Received: April 16, 2022 Published: May 20, 2022





is appropriate for describing interactions between opposing charges (e.g., protein–DNA association 49,50), though it can not (by construction) capture ion-induced attraction between polyanionic molecules. 51 To address this shortcoming, coarsegrained models that include explicit-ion representations have been developed to analyze ion-mediated attraction in DNA. 52,53 Explicit-ion models with coarse-grained RNA representations have also been successful in predicting biomolecular stability, 42,54 as well as the mechanisms 26,27 and energetics 39 of large RNA folding. At a higher level of spatial resolution, ion parameters are available for use with all-atom explicit-solvent simulations. 55-57 In various applications, these have provided interpretations of ensemble experimental data⁵⁸ and insights into the energetics of small RNA systems.^{59–61} While explicitsolvent techniques may be applied to larger systems, the associated computational requirements have limited the accessible time scales to microseconds. 62 As a result, there is not an all-atom model available for which it is tractable to directly connect the properties of diffuse ions with slow (millisecond) conformational processes in large-scale RNP assemblies.

To probe how diffuse ions influence conformational dynamics in biomolecular assemblies, we developed an all-atom (nonhydrogen atom) model that employs simplified energetics for each biomolecule, along with a transferrable effective potential for explicit monovalent (K⁺, Cl⁻) and divalent (Mg²⁺) ions. In this model, which we call SMOG-ion, an all-atom structurebased (SMOG) model^{63,64} is used to define intramolecular interactions, while ionic interactions are assigned nonspecific effective potentials and Coulomb electrostatics. The ion parameters were first refined based on comparison with explicit-solvent simulations of small model systems (rRNA helix and protein S6). A subset of the ion—RNA parameters were then further refined through comparison with an experimental measure of the excess ionic atmosphere for a prototypical rRNA fragment. While the parameters were defined based on experiments performed for a single system and concentration, we find the model accurately describes the concentrationdependent properties of the diffuse ionic atmosphere for multiple small RNA molecules. Building upon these benchmarks, we applied the model to simulate a bacterial ribosome in the presence of monovalent and divalent ions. We find that the free-energy barrier of a large-scale (~30 Å) conformational rearrangement (i.e., tRNA accommodation) is regulated by the diffuse ionic environment. In addition, the affinity of tRNA for the ribosome shows a clear ionic concentration dependence. Together, these calculations implicate a direct relationship between diffuse ions and the structural dynamics of this large biomolecular assembly.

METHODS

Structure-Based "SMOG" Model with Explicit lons. The SMOG—ion model is an all-atom structure-based "SMOG" model 63,64 with explicit electrostatics and an explicit representation of diffuse ions $(K^+, Cl^-, \text{and } Mg^{2+})$. Ionic interactions are defined in terms of Coulomb electrostatics and effective potentials. The potential energy may be described in terms of two components:

$$V = V_{\rm SMOG} + V_{\rm E} \tag{1}$$

 $V_{
m SMOG}$ refers to the all-atom structure-based potential energy, and $V_{
m E}$ describes the potential energy of all electrostatic interactions.

In the all-atom structure-based SMOG model (V_{SMOG}) , 63,64 all non-hydrogen atoms are explicitly represented and an experimentally

identified configuration is defined as the global potential energy minimum. The functional form of the SMOG model is given by

$$\begin{split} V_{\rm SMOG} &= \sum_{ij \in \rm bonds} \frac{\epsilon_{\rm b}}{2} (r_{ij} - r_{ij}^0)^2 + \sum_{ijk \in \rm angles} \frac{\epsilon_{\theta}}{2} (\theta_{ijk} - \theta_{ijk}^0)^2 \\ &+ \sum_{i \in \rm improper} \frac{\epsilon_{\chi \rm imp}}{2} (\chi_i - \chi_i^0)^2 \\ &+ \sum_{i \in \rm planar} \frac{\epsilon_{\chi \rm planar}}{2} \cos(2\chi_i - \pi) + \sum_{i \in \rm backbone} \epsilon_{\rm BB} F_D(\phi_i) \\ &+ \sum_{i \in \rm side \; chains} \epsilon_{\rm SC} F_D(\phi_i) + \sum_{ij \in \rm contacts} \epsilon_{\rm C} \left[\left(\frac{r_{ij}^0}{r_{ij}} \right)^{12} - 2 \left(\frac{r_{ij}^0}{r_{ij}} \right)^6 \right] \\ &+ \sum_{ij \notin \rm contacts} \left(\frac{C_{18}}{r_{ij}^{18}} - \frac{C_{12}}{r_{ij}^{12}} \right) \end{split}$$

where

$$F_{\rm D}(\phi_i) = [1 - \cos(\phi_i - \phi_i^0)] + \frac{1}{2}[1 - \cos(3(\phi_i - \phi_i^0))]$$

The ϕ_i^0 are given the values found in a preassigned configuration. r_{ij}^0 and θ_{ijk}^0 are assigned the corresponding values found in the Amber99sb-ildn force field, 65 as employed in a previous SMOG-AMBER model. 66 Interaction weights are assigned as defined in ref 64. Contacts are defined using the Shadow Contact Map algorithm 67 with a 6 Å cutoff and a 1 Å shadowing radius.

In contrast with previous $\bar{S}MOG$ models, we included a 12–18 potential for atom pairs that are not in contact in the experimentally defined structure. This was introduced in order to define an excluded volume potential that mimics that of the AMBER force field, without including a deep attractive well (Figure S1). With this approach, the steric representation provided by the model is consistent with the more highly detailed AMBER model, while introducing a minimal degree of nonspecific energetic roughness. The coefficients C_{18} and C_{12} were defined for each type of interaction based on fits to the corresponding 6–12 potentials in the Amber99sb-ildn force field (Figure S1).

The electrostatic representation $(V_{\rm E})$ includes direct Coulomb interactions $(V_{\rm coulomb})$, effective excluded volume potentials for diffuse ions $(V_{\rm ion-excl})$ and effective potentials that describe ionic solvation effects $(V_{\rm sol})$:

$$V_{E} = V_{\text{coulomb}} + V_{\text{ion-excl}} + V_{\text{sol}}$$

$$= \sum_{ij} \frac{q_{i}q_{j}}{4\pi\epsilon\epsilon_{0}r_{ij}} + \sum_{ij} \frac{A}{r_{ij}^{12}} + \sum_{ij} \left(\sum_{k=1}^{5} B^{(k)}e^{-C^{(k)}[r_{ij}-R^{(k)}]^{2}}\right)$$
(3)

 $V_{\rm coulomb}$ represents the direct Coulomb interactions between a pair of charges q_i and q_j with interatomic distance r_{ij} , ε is the dielectric constant for water (80) and ε_0 is the permittivity of free space. The partial charge of each atom was derived from the Amber99sb-ildn force field. ⁶⁵ Since the SMOG—ion model only includes non-hydrogen atoms, the partial charge of each hydrogen atom in the AMBER force field was added to the corresponding non-H atom.

The effective excluded volume of each diffuse (hydrated) ion is account for by $V_{\text{ion-excl}}$. Consistent with previous efforts to model explicit ions in a coarse-grained model, ⁵² pairwise potentials of the form $\frac{A}{r_{ij}^{12}}$ were used to define the excluded volume between ion i with atom j.

The parameter A is different for each type of interaction in the model (e.g., Cl–Cl, Cl–K, K–O, etc.). To simplify notation, subscripts are not shown. Following the protocol of Savelyev and Papoian, ⁵² the values of the parameters $\{A\}$ were obtained through refinement based on comparison with explicit-solvent simulations (see Supporting Information for details).

The term $V_{\rm sol}$ describes solvent-mediated ionic interactions, which manifest in the form of ionic shells. The functional form is the same as used previously, 52 where a sum of Gaussians describe the shells ($B^{(k)}$ <

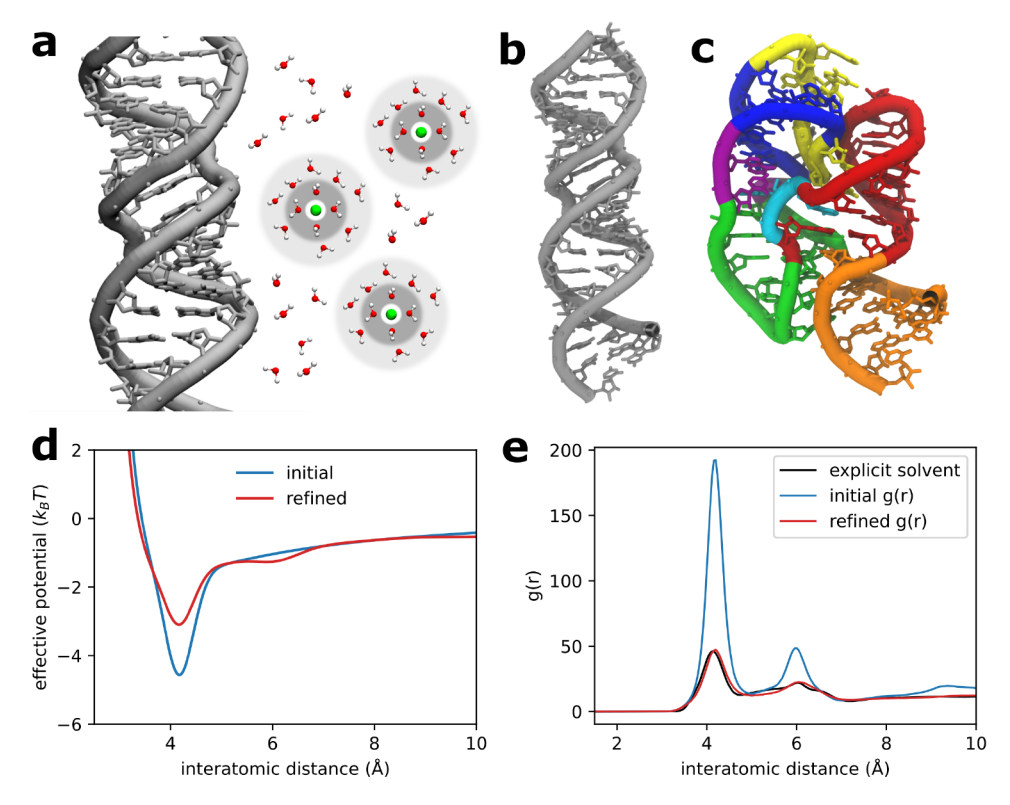


Figure 1. Describing the dynamics of diffuse ions: The SMOG—ion model. To study the influence of diffuse ions on large-scale molecular assemblies, we developed an all-atom model with simplified energetics (SMOG—ion) in which monovalent and divalent ions are explicitly represented. In this model, intramolecular interactions are defined by a structure-based model, 63,64 partial charges are assigned to each atom, and effective potentials are introduced to account for the effects of ion—ion correlations and hydration. (a) While chelated ions form strong interactions with biomolecules, diffuse ions (green beads) maintain hydration shells (gray rings) that prevent tight binding. (b) Structure of helix 44 (h44) of the ribosomal small subunit, which was used as a test system for initial parametrization of the model. (c) An rRNA 58-mer that was used for comparison and calibration against experimental measurements. (d) Potential for diffuse Mg^{2+} interactions with highly charged RNA oxygen atoms before (s0 parameters, blue) and after (s1 parameters, red) refinement against explicit-solvent simulations of h44. After refinement, the corresponding radial distribution function (e) agrees well with that obtained using the explicit-solvent model, which ensures the ionic shells are consistently described. For a list of modeled interactions, see Tables S1—S5. For comparison of g(r) for all interaction types, see Figure S5. After comparison with explicit-solvent simulations, minor adjustments to Mg^{2+} and K^+ interactions were subsequently introduced based on comparison with experiments for the 58-mer. The same content of the same consistency of the same co

0) and intervening barriers $(B^{(k)} > 0)$. For each type of interaction considered, up to five Gaussians were included to describe up to three (outer) ionic shells. The location $(R^{(k)})$ and width $(C^{(k)})$ of each Gaussian was set based on an initial fit to the corresponding radial distribution function. The amplitude of each Gaussian $(B^{(k)})$ was refined based on comparison with explicit-solvent simulations and experimental measurements (details in the Supporting Information). Consistent with the assignment of excluded volume parameters, unique Gaussian parameters were assigned to each type of modeled interaction. As a note, the parameters in our model are not concentration dependent. Since calculations and experiments have shown the strong concentration dependence of ionic chemical potentials for large changes in ionic strengths (0-5.5 m), 68 the parameters in the SMOG—ion model will likely need to be rerefined if one seeks to study higher ionic concentrations than those considered here.

Upon publication, the SMOG—ion model will be freely available through the SMOG 2 Force Field Repository (https://smog-server.org/smog2 – Force Field ID: AA_ions_Wang22.v1).

Calculating Preferential Interaction Coefficients. We calculated the preferential interaction coefficient of Mg^{2+} ions (Γ_{2+}) from simulations with the SMOG—ion model and used it as a metric to compare with experimental measurements. Γ_{2+} describes the "excess" number of Mg^{2+} ions that accumulate around an RNA molecule due to electrostatic interactions. ^{69–73} In the current study, Γ_{2+} was calculated by taking the difference between the total number of simulated ions $(N_{\mathrm{Mg}^{2+}})$ and the expected bulk value. The expected bulk number is the product of the bulk density $(\rho_{\mathrm{Mg}^{2+}})$ and the volume of the simulated box

 $(V_{\rm box}),^{114}$ such that $\Gamma_{2+}=N_{\rm Mg^{2+}}-\rho_{\rm Mg^{2+}}\times V_{\rm box}.$ To calculate the bulk density, the RNA fragment was first recentered in the box for each frame of the trajectory. The box was then partitioned into five equal-width (~140 Å) slabs. The average density of Mg^2+ was then calculated by excluding the central (RNA-containing) slab. For each system and ion concentration, the effective concentration was calculated for 20 independent replicas. The uncertainty in the concentration was defined as the standard deviation of the 20 replicate values. While simulating many replicas helped reduce the uncertainty (standard deviation of [MgCl_2] \sim 0.005 mM), due to the large dimensions of the simulated systems, this leads to a residual uncertainty of \sim 1 in $\rho_{\rm Mg^{2+}}\times V_{\rm box}$. This uncertainty is then propagated to Γ_{2+} .

When calculating Γ_{2+} , it was necessary to account for chelated ions, as well as the diffuse ionic environment. Since the SMOG—ion model was only parametrized to describe diffuse ions, strongly bound chelated (inner-shell) ions were assigned *a priori*. In the adenine riboswitch, there are five Mg²⁺ binding sites (Figure S2b) identified in the crystal structure (PDB: 1Y26). The However, the binding site of Mg3 is formed by crystallographic interactions and no divalent cation binding could be detected in the vicinity of this position through high-resolution NMR spectroscopy and titration methods. Accordingly, this chelated ion was not included in the current simulations. However, since the other four Mg²⁺ ions are found deep within the grooves of the RNA, they were defined to be harmonically restrained to their chelation pockets. To compare with experimental approaches, which report the number of diffuse and bound ions, the four chelated ions were included

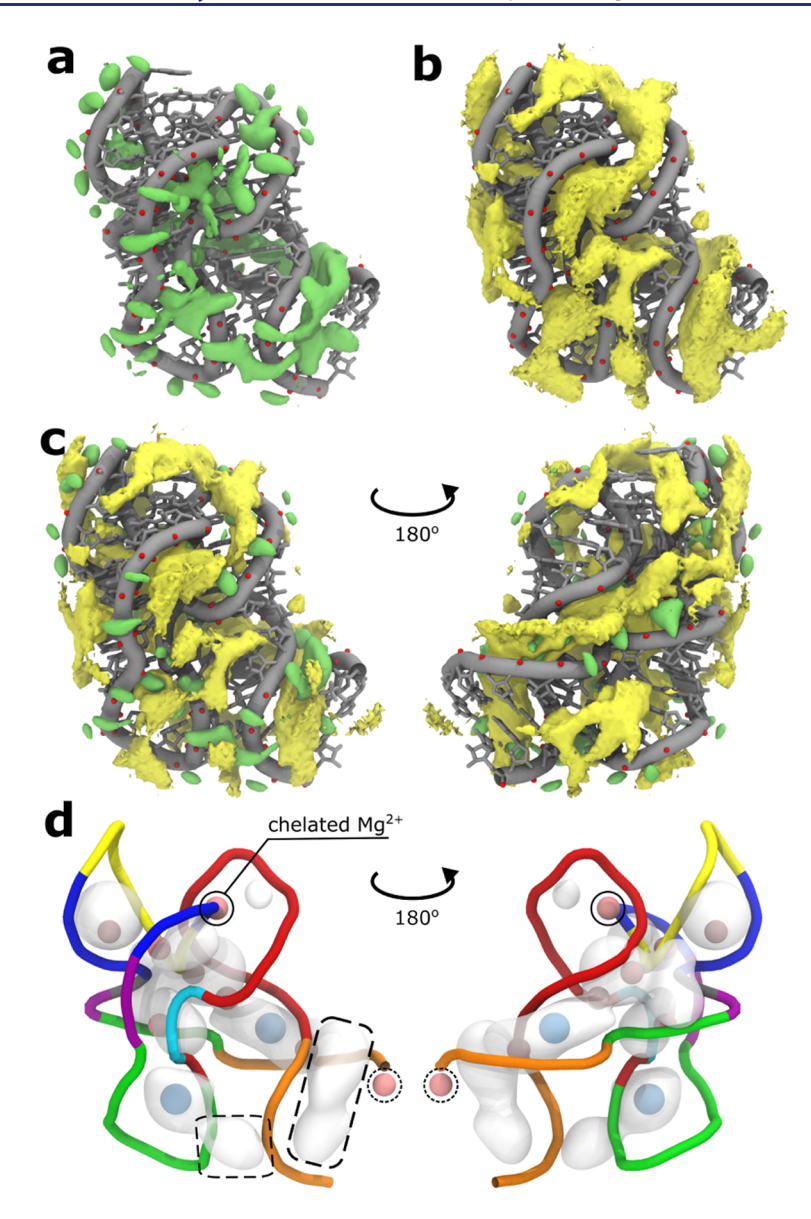


Figure 2. Characteristics of monovalent and divalent ion—RNA association. (a) Spatial distribution function (SDF) of diffuse Mg^{2^+} ions for the 58-mer ([MgCl₂] = 1 mM, [KCl] = 150 mM). The isosurface represents a 1.3 M concentration of Mg^{2^+} (1300-fold enrichment over bulk). (b) SDF for diffuse K^+ ions (isosurface at 1.3M). (c) The difference between the SDFs: $\Delta \rho = \rho_{Mg^{2^+}} - \rho_{K^+}$, where ρ_i is the SDF of ion type i. The green isosurface shows preferential association of Mg^{2^+} ions ($\Delta \rho$ = 1.3M), while yellow shows a preference for K^+ ions ($\Delta \rho$ = -1.3M). K^+ tends to populate the RNA grooves, consistent with its significant influence on the stability of secondary structure. Mg^{2^+} ions are dominant along the RNA backbone, consistent with their contribution to tertiary structure formation. Mg^{2^+} (d) SMOG—ion model predicts population of crystallographically reported ionic densities. SDF calculated for diffuse Mg^{2^+} ions (chelated ion not included) after applying a Gaussian filter. Isosurface shown for Mg^{2^+} concentration of 0.5 M. Crystallographically assigned nonchelated Mg^{2^+} ions (pink) and Mg^{2^+} ions (blue) are within the predicted regions of high diffuse Mg^{2^+} densities, except a solitary Mg^{2^+} ion near the terminal tail (dashed circle). In experiments, crystallographic contacts with the tail likely facilitate ion localization. In addition to predicting the crystallographic ions, there are two additional regions of high density (dashed boxes), which may further contribute to tertiary structure formation.

in our calculation of Γ_{2+} . Chelated ions in the 58-mer are described in the Results section.

RESULTS

To identify the effects of diffuse ions on the dynamics of biomolecular assemblies, we developed an all-atom model with simplified energetics and explicit ions (K^+, Cl^-, Mg^{2+}) , which we call SMOG—ion. An all-atom structure-based (SMOG) model 63,64 with explicit charges defines the biomolecular energetics. Ionic interactions are defined by Coulomb electro-

statics and effective potentials ($V_{\rm E}$, eq 3). The "structure-based" terms explicitly favor a predefined biomolecular structure, while the effective potentials ensure that the local distribution of ionic species is consistent with *in vitro* measurements. After describing performance benchmarks and parametrization, we demonstrate how this model may be used to isolate the influence of diffuse ions in a molecular assembly. Specifically, we compare the dynamics of the ribosome with multiple variants of the model, which reveals the direct impact of diffuse ions on the kinetics of a

large-scale conformational transition that is central to protein synthesis.

Simplified Model Reproduces in Vitro Ionic Distribution. To parametrize the SMOG-ion model, we first refined the interaction weights based on comparisons with explicit-solvent simulations of multiple systems (Figure 1 and Figure S3) for a single ionic composition ([MgCl₂] \approx 10 mM, [KCl] \approx 100 mM). The explicit-solvent simulations used the Amber99sbildn⁶⁵ force field with Mg²⁺ parameters described by Åqvist⁵⁵ and monovalent ion (K+ and Cl-) parameters of Joung and Cheatham. 56 We refined the ion-ion, ion-RNA, and ionprotein interactions in our model using the procedure of Savelyev and Papoian,⁵² where linear parameters in the Hamiltonian are iteratively updated through use of a firstorder expansion of the partition function (eq S2b). With regards to nomenclature, "sN" denotes the model parameters after refinement step N. The initial parameters (s0; Figure 1d, blue curve) were estimated based on inspection of radial distribution functions (RDFs) calculated from explicit-solvent simulations (Figure S4a). With the s0 parameters, the positions and widths of the peaks in each RDF were consistent with the explicitsolvent model (Figure 1e, blue curve), though there were significant differences in the heights of each peak. We then sequentially refined the ion-ion, ion-RNA, and ion-protein interactions (i.e., s1 parameter set; details in Supporting Information). The s1 model produced RDFs for Mg²⁺, K⁺, and Cl⁻ that exhibited excellent agreement with those obtained with the explicit-solvent model (Figures 1e and S5). This initial refinement ensures the description of outer ionic shells is comparable to predictions by more highly detailed models.

In the second stage of refinement, a subset of the ion parameters was adjusted based on comparison with experimental measures of diffuse ionic distributions. For this, the preferential interaction coefficient of Mg²⁺ ions (Γ_{2+}) was calculated from simulations of a 58-nucleotide rRNA fragment (Figure 1c and Figure S2a). For consistency with the experimental conditions, we simulated the 58-mer with [MgCl₂] = 1 mM and [KCl] = 150 mM. Even though the s1 model parameters recapitulate the ionic distributions predicted by the explicit-solvent model (Figure 1e), Γ_{2+} was significantly underestimated for the 58-mer. Specifically, the predicted value of Γ_{2+} was 2.2 \pm 0.6, whereas the experimental value was 10.4.

Since the underestimation of Γ_{2+} indicated an imbalance between K⁺ and Mg²⁺ association strengths with RNA,³ we introduced minor changes to the Mg^{2+} and K^{+} interactions with highly electronegative RNA atoms. In explicit-solvent simulations of RNA, excess K+ ions are frequently partially dehydrated, which can artificially amplify the effective strength of K+-RNA interactions. 77,78 This observation is at odds with NMR studies that have reported most K⁺ ions tend to remain fully hydrated.¹⁷ Since the s1 parameter set was based on comparison with an explicit-solvent model, we removed the effective potential that stabilizes short-range (first outer shell) interactions between diffuse K⁺ ions and electronegative (q < -0.5) O and N atoms (yielding the s2 parameter set). While this increased Γ_{2+} from 2.2 (s1) to 6.4 (s2), the persistent underestimation of Γ_{2+} suggested the effective potential for Mg^{2+} was also insufficiently stabilizing. Since Γ_{2+} is predominantly influenced by the distribution of diffuse Mg^{2+} ions around highly electronegative atoms, 39,77 we introduced a small increase to the stability of these interactions in our model. Using estimates obtained from an energetic-based reweighting strategy, 115 we tested the effect of increasing the short-range

(outer shell) ${\rm Mg^{2+}}$ interaction by 0.16 ε (s3 parameter set). With this change, $\Gamma_{2+} = 9.5 \pm 0.7$, which is comparable to the experimental value of 10.4. Due to the uncertainty in the calculated Γ_{2+} values (see Methods), we decided to terminate the refinement process upon reaching this level of agreement. For all subsequent analysis, we used the s3 parameter set, which will simply be referred to as the SMOG—ion model.

Spatial Partitioning of Diffuse Ionic Species. Our simplified model predicts condensation and spatial partitioning of ionic species, which is consistent with monovalent and divalent ions contributing differentially to the stability of secondary and tertiary structure in RNA. The predicted spatial distributions (Figure 2) for the 58-mer are generally corroborated by prior crystallographic analysis and explicit-solvent simulations. In terms of biomolecular structure, K⁺ ions primarily populate the major grooves of the RNA, while Mg²⁺ ions appear to bridge interactions associated with tertiary structure.

Before comparing the predicted ionic distributions with crystallographic data, it is necessary to describe the experimental assignment of ions. The crystal structure of the 58-mer⁷⁶ (PDB ID: 1HC8) contains two asymmetric protein—RNA assemblies in the unit cell, and there are eight Mg^{2+} assignments that are common (Figure 2d, pink beads). Of these common assignments, Poisson—Boltzmann calculations indicate one is likely to be bound (Figure 2d, circled; binding free energy $\Delta G_{\rm bind} = -4.8$ kcal/mol, ref 79). On this basis, the system is typically described as possessing a single chelated Mg^{2+} ion. Since our model was parametrized for the study of diffuse ions, harmonic interactions were introduced to maintain the position of this single chelated Mg^{2+} ion. There is also a chelated K⁺ (described in ref 76) that we restrain to its binding site. Finally, the crystal structure has two nonchelated Os³⁺ ions that were not included in our simulations.

The SMOG-ion model predicts high local concentrations of Mg²⁺ ions that coincide with the crystallographically resolved positions of nonchelated multivalent ions. Specifically, the model predicts regions of high Mg²⁺ density that overlap with six of the seven nonchelated Mg²⁺ positions (Figure 2). The only outlier is positioned near the terminal guanosine-5'-triphosphate residue (Figure 2d, dashed circle). In the simulations, mobility of the tail impedes ion association. In contrast, in the experimental structure, crystallographic contacts with the tail likely reduce the flexibility, which in turn can facilitate a higher ion density. The model also predicts high Mg²⁺ densities that overlap with the experimentally assigned positions of both Os³⁺ ions (Figure 2d, blue beads). Overall, consistency between the predicted SDFs and crystallographic analysis suggests that our model provides an accurate description of the local ionic environment.

The SMOG—ion model implicates differential contributions of monovalent and divalent ions to the stability of RNA. In our model, diffuse K^+ and Mg^{2+} ions both populate the major groove of double-stranded RNA helices (Figure 2a,b), as predicted by explicit-solvent simulations. This shows how both ionic species can contribute to the stability of secondary structure in RNA, a property also predicted by coarse-grained models. Consistent with explicit-solvent simulations, we also find that Mg^{2+} ions accumulate around each backbone phosphate group (Figure 2c, green). As demonstrated in simulations with coarse-grained models, 26,27,39 the observed distributions reinforce the notion that diffuse Mg^{2+} ions are a primary contributor to tertiary structure formation in RNA. Interestingly, the model

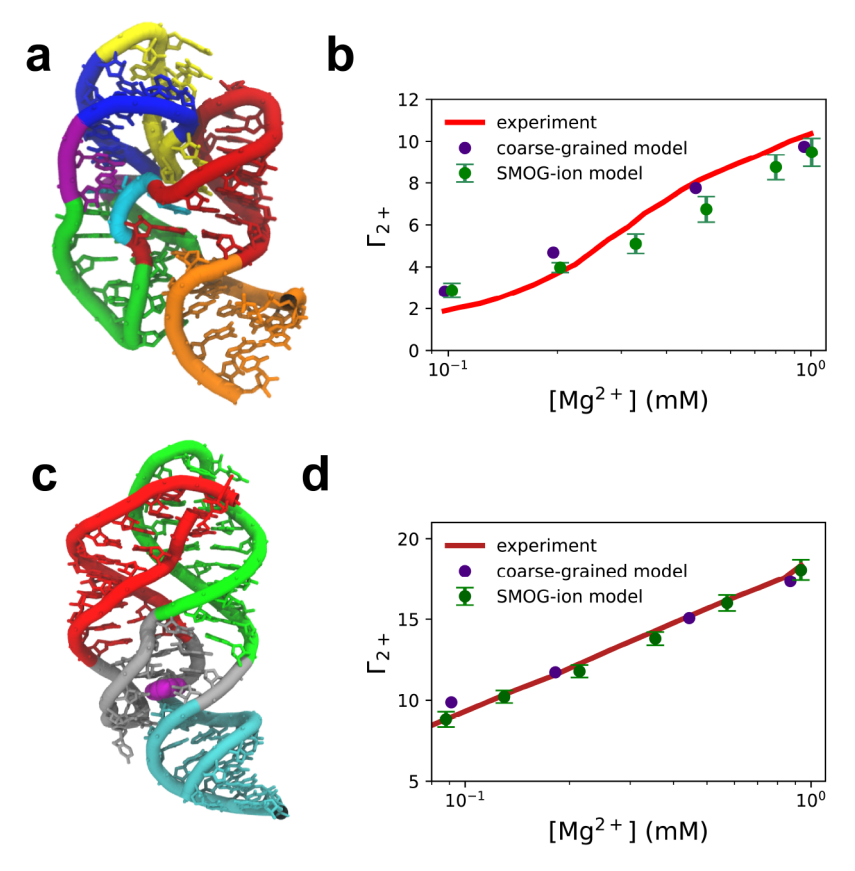


Figure 3. Simplified model captures concentration-dependent ion association. (a) Tertiary structure of the 58-mer rRNA fragment⁷⁶ (colored as in Figure 1c). (b) Preferential interaction coefficient (Γ_{2+}) for the 58-mer ([KCl] = 150 mM), shown for the SMOG-ion model, previous experimental values⁷² and predictions from a coarse-grained model of Nguyen et el.³⁹ While our model was parametrized based on comparison with the experimental value of Γ_{2+} at [MgCl₂] = 1 mM, the predicted concentration dependence (green dots) follows the experimental behavior (red curve) and agrees well with previous predictions from the coarse-grained model³⁹ (purple dots). (c) Tertiary structure of the adenine riboswitch, ⁷³ colored as in Figure S2b. (d) The value of Γ_{2+} for the adenine riboswitch ([KCl] = 50 mM), obtained with the SMOG-ion model (green dots), experimental measurements⁷³ (dark red curve), and the coarse-grained model of Nguyen et al.³⁹ (purple dots). There is excellent agreement between the values, even though the riboswitch was not used for model parametrization, and our model parameters were established using benchmark systems at higher value of [KCl] (100–150 vs 50 mM). Accordingly, these comparisons support the transferrability of the model to other RNA systems and ionic concentrations. Error bars in (b) and (d) represent the standard deviation of Γ_{2+} calculated from 20 replicate simulations.

predicts two regions of high Mg²⁺ density that do not coincide with assigned ion positions (Figure 2d, boxed regions). Both of these regions span RNA segments that are distant in sequence. These high-density regions further suggest how Mg²⁺ ions may facilitate higher-order structure formation in RNA.

Model Captures Concentration-Dependent Ionic **Atmosphere.** Before applying the SMOG-ion model to a large biomolecular assembly, we evaluated its transferability by comparing the concentration dependence of Γ_{2+} with experimental values and those recently obtained with a coarsegrained model.³⁹ For this, we considered two different RNA molecules: the 58-mer rRNA fragment⁷² and an adenine riboswitch.⁷³ Comparing concentration-dependent values of Γ_{2+} allows one to ask whether the modeled parameters appropriately describe the competition of ionic species. It is important to note that the ion-RNA interaction strengths were assigned based on comparison with explicit-solvent simulation and a single experimental value of Γ_{2+} . Accordingly, calculating Γ_{2+} values for multiple systems over a range of ion concentrations represents a blind test of the transferability of the model.

We first compared with previously predicted and experimental values of Γ_{2+} for the 58-mer rRNA (Figure 3a,b). While the SMOG-ion model was calibrated using the 58-mer

with $[MgCl_2] = 1$ mM and [KCl] = 150 mM, we find it accurately predicts the change in Γ_{2+} as a function of $[MgCl_2]$. Over the studied concentrations ($\sim\!0.1-1$ mM), the experimental Γ_{2+} values change by 8.0, whereas the model predicts a change of 6.6. There is a systematic underestimation (\sim 1) of the Γ_{2+} values at higher ion concentrations, though the statistical uncertainty in the theoretical values is comparable to this difference (Figure 3b). In addition, the values of Γ_{2+} predicted by the SMOG-ion model agree well with those obtained with a leading coarse-grained model³⁹ (Figure 3b, purple dots). It is important to note that this analysis was performed for a hyperstable variant of the rRNA (U1061A), and comparisons are limited to higher experimental ionic concentrations. Since this RNA is known to remain folded under these conditions, this set of comparisons allows us to specifically assess the accuracy of the ion parameters, in a manner that is independent of the biomolecular potential. However, it is possible that the experimental values also reflect concentration-dependent effects on RNA structure that are not addressed here. With these experimental and statistical uncertainties in mind, one may consider the residual differences between Γ_{2+} values to be minor.

Applying the model to the adenine riboswitch (with ligand bound) (Figure 3c) demonstrates the transferability of the ion parameters. Since the riboswitch was not utilized for any aspect

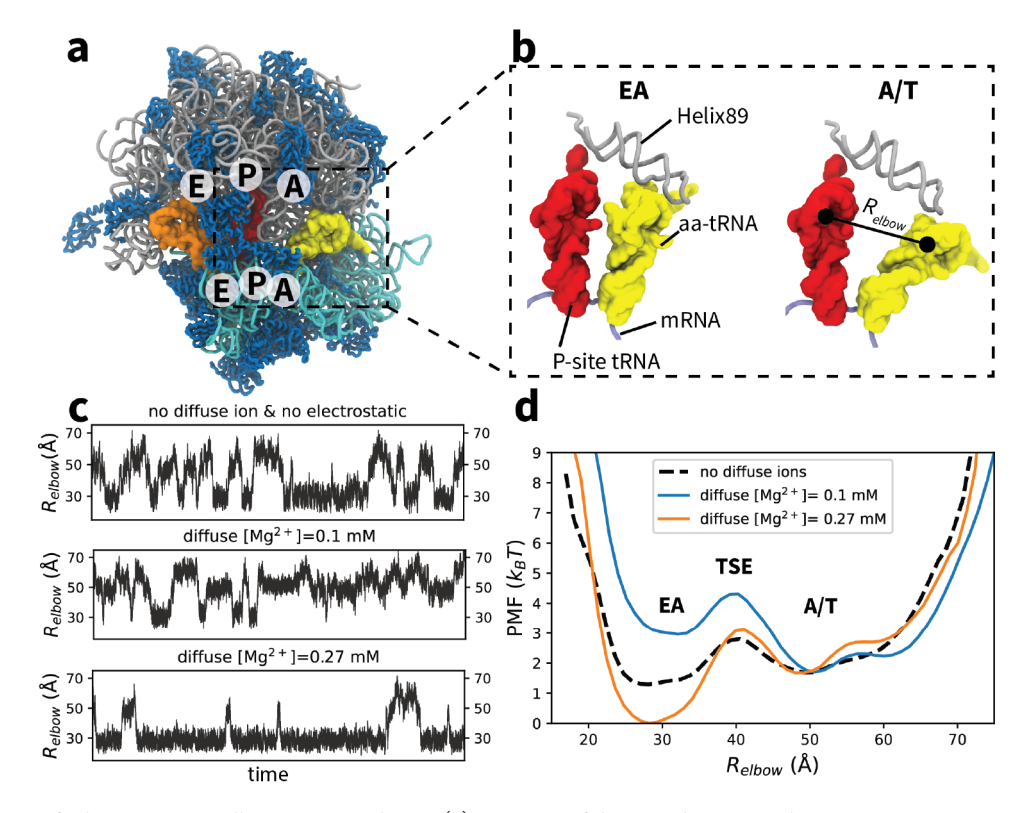


Figure 4. Diffuse ions facilitate aa-tRNA elbow accommodation. (a) Structure of the 70S ribosome with 23S rRNA in gray, 16S rRNA in cyan and proteins in blue. The ribosome is shown in complex with an A/T-configured aa-tRNA (yellow), P-site tRNA (red), E-site tRNA (orange), and mRNA (purple). (b) aa-tRNA elbow accommodation involves a ~ 25 Å rearrangement between A/T and EA configurations. $R_{\rm elbow}$ is the distance between the O3' atoms of U60 in the aa-tRNA and U8 in the P-site tRNA. (c) Representative trajectories of simulations using all-atom structure-based models with different treatment of electrostatics and diffuse ions. In all systems, spontaneous transitions are observed between the A/T and EA ensembles. The electrostatics-free and ion-free model⁸⁴ (top) is used as a reference, where there is roughly equal probability of adopting either end point. Depending on the ionic concentration (middle, bottom), the range of accessible tRNA positions is shifted. (d) The potential of mean force (PMF = $-k_B T \ln(P)$) for each model. In the absence of electrostatics and diffuse ions (dashed line), the free energies of the A/T to EA ensembles are comparable. When explicit electrostatics is included, and [KCl] = 100 mM with a concentration of 0.1 mM for diffuse Mg²⁺ ions (blue), the landscape is shifted toward the A/T ensemble. At higher concentrations of diffuse Mg²⁺ ions (orange curve and Figure S7) the free-energy of the transition state ensemble (TSE) is reduced and the landscape is shifted toward the EA ensemble, which corresponds to aa-tRNA binding of the ribosome.

of parameter refinement, it serves as a blind test of the predictive capabilities of the model. In addition, the experiments were performed at lower values of [KCl] for the adenine riboswitch than for the 58-mer (50 mM 73 vs 150 mM 72). Accordingly, this comparison implicitly evaluates the predicted concentration-dependent influence of monovalent ions on Mg $^{2+}$ -RNA association. We find that the predicted Γ_{2+} values agree very well with the experimental measurements, where the level of agreement is comparable to predictions from the coarse-grained model of Nguyen et al. (Figure 3d). Combined with our analysis of the 58-mer, this demonstrates the ability of the SMOG—ion model to accurately estimate the energetics and association of diffuse ions.

Diffuse lons Control tRNA Kinetics on the Ribosome. After benchmarking the SMOG—ion model, we used it to investigate how diffuse ions contribute to a large-scale conformational transitions in the ribosome: aminoacyl-tRNA (aa-tRNA) accommodation. After delivery of aa-tRNA to the ribosome by EF-Tu, the accommodation process allows the tRNA to fully bind the ribosome, where this step is responsible for proofreading the incoming tRNA molecule. Here, we simulated the first step of aa-tRNA accommodation, called elbow accommodation (Figure 4A). This large-scale (~20–30 Å) conformational rearrangement has been extensively studied using electrostatics-free models 83–86 and implicit-ion models.

Explicit-solvent simulations have also been used to calculate diffusion coefficients^{88,89} and to perform nanosecond-scale targeted simulations of this process. 90 This body of work has shown that Helix 89 (H89) introduces a pronounced sterically induced free-energy barrier 83-86 that can be amplified by direct electrostatic interactions between aa-tRNA and H89.87 Electrostatic and solvent interactions between tRNA and H89 can also introduce energetic roughness that leads to coordinate-dependent diffusive properties of tRNA.⁸⁹ There have also been experimental insights into the roles of ions. For example, anomalous scattering data has been used to identify the composition of bound ions on the ribosome⁹¹ and changes in solvent conditions have been shown to dramatically alter the kinetics of accommodation. 15,92 Here, the SMOG-ion model provides complementary insights into tRNA dynamics by specifically isolating the influence of diffuse ions on the kinetics of accommodation.

To examine the role of diffuse ions during aa-tRNA elbow accommodation, we performed simulations of the complete 70S ribosome using the SMOG-ion model, and compared the dynamics for different ionic strengths. Consistent with earlier analysis, ⁸⁴ we calculated the free-energy barrier as a function of $R_{\rm elbow}$: the distance between the O3′ atoms of U60 of aa-tRNA and U8 of P-site tRNA. In these simulations, spontaneous transitions between the A/T ($R_{\rm elbow} \sim 50$ –60 Å) and EA

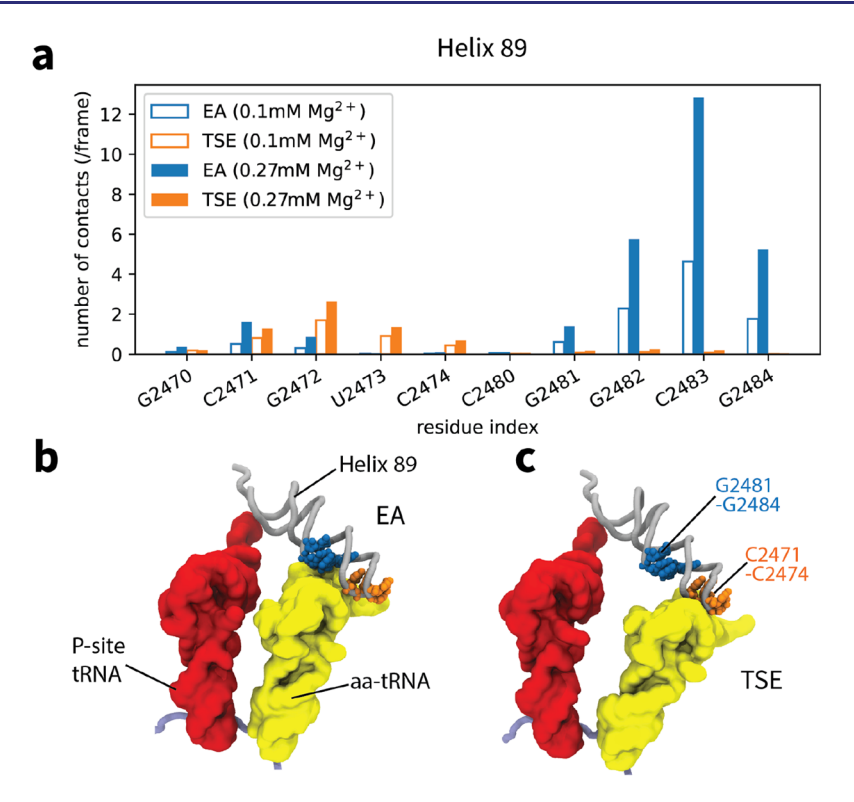


Figure 5. ${\rm Mg}^{2^+}$ -mediated interactions explain changes in the energy landscape. (a) The average number of ${\rm Mg}^{2^+}$ -mediated interactions between aatRNA and H89, calculated for the EA ensemble (blue) and Transition State Ensemble (TSE: orange). Solid bars correspond to a diffuse ${\rm Mg}^{2^+}$ concentration of 0.27 mM, while empty bars correspond to 0.1 mM. In the TSE (c), transient ion-mediated interactions are formed between the aatRNA and the stem loop of H89 (C2471–C2474; orange residues). There is also a slight increase at higher concentrations of ${\rm Mg}^{2^+}$, which is consistent with the smaller free-energy barrier (Figure 4). Upon reaching the EA ensemble (b), ion-mediated interactions with the stem loop dissolve, while a larger number of ion-mediated interactions is then formed with the base of H89 (G2481–G2484; blue residues). There is also a sharp increase in the number of ion-mediated interactions at higher concentrations, consistent with the larger energetic effect of ions on the free energy of the EA (ribosome-bound) ensemble.

ensembles ($R_{\rm elbow} \sim 30$ Å) are observed (with ions present, or absent). When the electrostatics-free model is used (labeled "SMOG model" in Table S5), the free energy of the A/T and EA ensembles is comparable (Figure 4d, black). When electrostatics and monovalent ions ([KCl] = 100 mM) are included, along with bound Mg²⁺ ions (no diffuse Mg²⁺), the energy landscape is shifted toward the A/T ensemble, and there are only transient excursions in the direction of the EA ensemble (Figure S6). This shows how, even when monovalent ion screening is accounted for, there is strong electrostatic repulsions between the aa-tRNA and the ribosome. When the bulk concentration of diffuse Mg²⁺ ions is only 0.1 mM, aa-tRNA is found to stably populate both the A/T and EA ensembles, where the free-energy barrier between A/T to EA is $\sim 3 k_B T$ (Figure 4d, blue). Interestingly, this is slightly larger than the barrier obtained with the electrostatic-free model ($\sim 1.5 k_B T$), illustrating the residual RNA-RNA repulsion that is present under these conditions. When the bulk concentration of Mg²⁺ ions is increased to 0.27 mM, the free-energy barrier is reduced by $\sim 1.5 k_B T$ (Figure 4d, orange), consistent with further attenuation of electrostatic repulsions between H89 and aa-tRNA. The EA ensemble is also stabilized at this higher concentration of Mg^{2+} (Figure 4d, orange). When the concentration of diffuse Mg^{2+} ions is further increased, aa-tRNA is observed to strongly favor the EA ensemble over A/T (Figure S7), where the dynamics is suggestive of a downhill energy landscape. Together, these results illustrate the strong dependence of aa-tRNA kinetics and

thermodynamics on the precise concentration of diffuse Mg²⁺

While the current analysis reveals a clear energetic role of diffuse ions, these observations suggest many interesting avenues for continued investigation. For example, similar to a coarse-grained model,³⁹ one may extend the SMOG-ion model to describe binding of chelated ion, which would be necessary to account for their effects on RNA stability. In this regard, while the flexibility of the ribosome is well described by the SMOGion model (Figure S8), the overall stability will need further characterization and parametrization. That is, it will be important to better understand the scale of stabilization imparted by the combination of structure-based energetics and nonspecific electrostatic interactions. Resolving this limitation can also open the possibility of identifying localized disorder events, which would have the potential to influence substeps of elongation. Another feature of the present model is that it was tuned so that the A/T and EA ensembles are of comparable free-energy in the absence of electrostatics. This strategy was applied, in order for the ion-free simulations to provide a reference distribution, against which the perturbative effects of ionic concentration changes could be compared. In future models, one may envision relaxing the explicit stability of the accommodated (EA) basin. Such a change would shift the landscape toward the A/T ensemble, where higher ionic concentrations (i.e., closer to biological values) will likely be necessary for favorable A-site binding to occur. As a final example, it will be interesting to characterize the detailed

influence of Elongation Factor-Tu when diffuse ions are present. While screened-electrostatic models have shown that EF-Tu can facilitate the accommodation process through steric effects, 87 it is possible that diffuse ions will further modulate this influence on the incoming tRNA molecules.

How Ion-Mediated Interactions Regulate tRNA-Ribo**some Dynamics.** To provide structural insights into the mechanisms by which diffuse ions can alter the energy landscape of the ribosome, we analyzed the statistical properties of ionmediated interactions. Specifically, we identified all Mg²⁺ -mediated interactions that are formed between highly negatively charged atoms of the aa-tRNA and rRNA of the large subunit (LSU). Here, an interaction is defined as "ionmediated" if an Mg²⁺ ion is simultaneously within 5 Å of the aatRNA and LSU. To connect this analysis with the observed changes in the free-energy landscape (Figure 4d), we evaluated the average number of ion-mediated interactions formed in the EA, transition state (TSE) and A/T ensembles. This reveals several ion association "hot spots" on the ribosome that form significant numbers of ion-mediated contacts with the aa-tRNA molecule. We also find specific regions for which there are clear concentration-dependent interactions with tRNA, which provides a molecular explanation for the ion-dependent effects on accommodation kinetics.

The largest number of ion-mediated interactions are formed between the tRNA molecule and H89. As noted above, the excluded volume of H89 has been shown to introduce a sterically induced free-energy barrier during elbow accommodation,⁸⁴ where direct electrostatic interactions can amplify the barrier height.⁸⁷ Here, we find distinct sets of ion-mediate interactions are transiently formed with H89 during the accommodation process (Figure 5). At the early stages of accommodation, the aatRNA approaches the stem loop of H89 (C2471-C2474; orange in Figure 5c). Upon reaching the TSE, the aa-tRNA forms up to around three ion-mediated interactions with individual residues (e.g., C2472), where the number of interactions increases with the concentration of divalent ions. This is consistent with the observation that the free-energy barrier is smaller (reduced by 1.5 k_BT) for the higher concentration of diffuse ions (Figure 4d; blue vs orange curves). After the tRNA overcomes the free-energy barrier and enters the EA ensemble, these transient ion-mediated interactions dissolve, which is expected due to the increased distance between the stem loop and the tRNA molecule.

As the tRNA molecule enters the EA ensemble, a second set of ion-mediated interactions is formed. Specifically, there is a large increase in the number of interactions with the base of H89 (Figure 5b; G2481–G2484 in blue). A small number of contacts is also formed with H92 (Figure S9). Together, there are more ion-mediated interactions formed in the EA ensemble than in the TSE. The number of contacts formed in the EA ensemble also exhibits a stronger concentration dependence, where an individual residue (C2483) gains up to eight additional ionmediated interactions at higher concentrations. This stark concentration dependence of ion-mediated contacts rationalizes the more pronounced increase in stability of the EA ensemble (\sim 3 k_BT), relative to changes found for the TSE (\sim 1.5 k_BT).

In addition to the influence of H89, our simulations also implicate a minor influence of the L11 stalk on accommodation kinetics. The L11 stalk is a flexible and extended region that is located at the periphery of the ribosome (Figure S10), and it is essential for the binding of elongation factors (EF-Tu and EF-G). $^{93-96}$ It is also the binding site of thiostrepton, which inhibits translocation by preventing phosphate release. 97,98 Previous simulations have shown that changes in L11 flexibility can impact the free-energy barrier associated with the elbow accommodation, 85 where L11 is able to confine the aa-tRNA motion within the A/T ensemble. To complement this effect, we find that Mg²⁺-mediated interactions between tRNA and L11 are more common in the A/T ensemble and TSE (Figure S11). In the EA ensemble, ion-mediated interactions with L11 are rare, due to the long distance between these structural elements. At higher concentrations, we find a modest increase in the number of ion-mediated interactions in the TSE (\sim 0.3) and a marginal decrease in the A/T ensemble (\sim 0.15). Together, these small changes may further contribute to the apparent reduction of the free-energy barrier at higher Mg²⁺ concentrations (Figure 4d).

DISCUSSION

Strategies for Studying Diffuse lons. The accuracy of ionic models is often evaluated based on studies of the adenine riboswitch and 58-mer rRNA. The reason for this choice is that high-quality experimental measures are available that describe the distribution of monovalent (K+ and Cl-) and divalent (Mg²⁺) ions around these RNA molecules.^{72,73} As described in the results, even though parametrization was based on experimental comparisons for a single ionic concentration, we find that the SMOG-ion model is able to capture the experimentally measured concentration dependence of Γ_{2+} for both systems. In terms of these common benchmarks, the SMOG-ion model provides a level of agreement that is comparable to other available models. Lammert et al. found that explicit-solvent simulations of the 58-mer⁸¹ overestimated Γ_{2+} by 2-3. However, due to the small system size in that study, there was a significant uncertainty in the calculated bulk ion concentration. In terms of coarse-grained approaches, Nguyen et al.³⁹ used theory based on the reference interaction site model to develop effective potentials for divalent ions. This representation was able to predict Γ_{2+} to within a value of 1 for both systems (Figure 3), which is comparable to the accuracy of SMOG-ion. While their use of pairwise effective potentials is similar to our approach, that model employed an implicit representation of monovalent ions. As a result, it was not tractable to calculate Γ_{2+} for the lowest concentrations of Mg²⁺ reported by Nguyen et al, since this would necessitate the use of a prohibitively large system of monovalent ions. Γ_{2+} values have also been accurately predicted using a generalized Manning condensation model proposed by Hayes et al. 99 Overall, we find that the SMOG-ion model is able to predict Γ_{2+} with accuracy that is comparable to leading theoretical models.

While numerous models can accurately predict experimental Γ_{2+} values, each is suited to address specific physical questions. In coarse-grained models developed by Thirumalai and colleagues, 26,27,39,42,54 a major focus has been to predict iondependent folding dynamics of large RNA molecules. Since folding can be described well with coarse-grained representations, 100 three-site models have been appropriate for those purposes. In the study of Nguyen et al., 39 an objective was to understand the dynamics of chelated ions during folding, which necessitated the proper treatment of inner-shell interactions with Mg²⁺. In the study of Lammert et al., 81 explicit-solvent simulations were used to identify how small-scale (short time) structural fluctuations were correlated with individual ion association events. With this finely detailed question in mind, a higher-resolution model was warranted. In contrast, Hayes et al. 99 focused on more general questions pertaining to the utility

of Manning theory to quantitatively predict ion condensation in asymmetric molecular systems, where an intermediate-resolution model is suitable.

Here, our aim is to study structural dynamics that involve transient formation of ion-mediated interactions. As an initial application, we have described how transient ion-association events are correlated with large-scale ($\sim 30 \, \text{Å}$) rearrangements of tRNA in the ribosome. Since numerous studies have shown that detailed steric interactions strongly influence the dynamics of tRNA in the ribosome, it was necessary for the SMOG—ion model to employ an all-atom representation of the biomolecules, while coarse-graining over the solvent.

Modeling the Factors That Control Biomolecular **Assemblies.** A major challenge in the study of ribonucleoprotein assemblies has been to precisely describe the influence of ions during large-scale conformational transitions. While there are efforts to refine ion parameters for use with explicit-solvent models, the large size of RNP assemblies (often MDa scales), combined with the slow time scales (microsecond-millisecond-second), makes direct simulation of the dynamics intractable with conventional models. In an effort to bridge our understanding of large-scale dynamics and ionic effects, we propose the SMOG-ion model, which is far less computationally expensive than explicit-solvent simulations. Due to the simple functional form, these simulations scale to thousands of compute cores for large assemblies (Figure S12), and they can be performed effectively using modern GPU resources. 101 With these levels of performance, modest-sized compute clusters are sufficient to perform simulations that describe millisecond effective time scales for MDa-scale assemblies. Accordingly, it is now becoming feasible to explore the impact of ions on largescale conformational rearrangements.

For the SMOG-ion model, all-atom resolution was employed since previous studies have repeatedly shown how sterically induced free-energy barriers can limit the kinetics of the ribosome. For example, multibasin structure-based models have demonstrated how the steric composition of the A-site finger controls the scale of the free-energy barrier associated with A/P hybrid formation. 102 During P/E hybrid formation, similar models have shown that the kinetics depends critically on the precise steric representation of the N-terminal tail of protein L33. 103 In these examples, direct perturbations to the steric representation in the model revealed the central influence of excluded volume. Since the contribution of sterics will be robust, so long as atomic resolution is included, it is expected that the positions of these barriers will also be robust to the energetic details of the model. However, by applying more energetically complete models, such as the SMOG-ion model, future studies will be able to further delineate the factors that control the scale of each barrier, and therefore the biological kinetics.

To complement the insights provided by the SMOG—ion model, explicit-solvent simulations and quantum mechanical methods can provide highly detailed descriptions of biomolecular interactions within larger assemblies. For the ribosome, explicit-solvent models have been widely used to quantify energetics of bimolecular binding events, ¹⁰⁴ or small-scale (e.g., single-residue) structural rearrangements. ¹⁰⁵ In other studies, they have been used to quantify the stabilizing interactions between different components of the ribosome, which have included studies of the L1 stalk, ^{106,107} interactions between the 3'-CCA tail of tRNA and its binding sites, ¹⁰⁸ as well as between tRNA and the ribosome, ¹⁰⁹ synthetases ¹¹⁰ and elongation factors. ¹¹¹ At an even higher level of resolution, quantum

mechanical techniques are available to study chemical reactions. 112,113

The stark differences between simplified/coarse-grained models and explicit-solvent techniques often make it difficult to integrate the results within a common quantitative framework. Here, we present a model that is substantially more energetically detailed than traditional structure-based models, while also being far simpler than explicit-solvent models. We anticipate that these intermediate-resolution models will help establish a more comprehensive understanding of RNP dynamics that will bridge the gap between detailed insights arising from explicit-solvent simulations and larger-scale processes that can be described by coarse-grained techniques. For example, one may use high-resolution methods to quantify precise energetic features (e.g., binding energetics, pH effects, etc.) and then encode these features into a SMOG-ion model variant. Through this, it would be possible to identify the effects of these localized interactions on larger-scale motions. Thus, building on the present results, one may methodically construct a comprehensive physical-chemical model that bridges disparate length and time scales.

CONCLUSIONS

Attributing specific roles to diffuse ions in ribonucleoprotein assemblies has remained elusive. While there has been notable progress in the study of monomeric systems and RNA folding,² unambiguously identifying specific physical-chemical effects of diffuse ions in assemblies continues to be challenging. As a step in this direction, we developed and employed a model that provides an explicit treatment of non-hydrogen atoms and ions, while providing an implicit treatment of solvent. We find that our model is able to capture experimental measures of the ionic environment for prototypical RNA systems, which motivated our application to a more complex system: the ribosome. By comparing the dynamics with a range of theoretical representations, we identify how diffuse-ion-mediated interactions can coordinate a large-scale rearrangement in the ribosome. With this foundation, the study provides a framework for identifying the ways in which diffuse ions help regulate the dynamics of complex biomolecular assemblies.

ASSOCIATED CONTENT

Supporting Information

The Supporting Information is available free of charge at https://pubs.acs.org/doi/10.1021/jacs.2c04082.

Additional computational details, methods, and figures (PDF)

AUTHOR INFORMATION

Corresponding Authors

Udayan Mohanty — Department of Chemistry, Boston College, Chestnut Hill, Massachusetts 02467, United States;
orcid.org/0000-0002-8778-974X; Email: mohanty@bc.edu

Paul C. Whitford — Department of Physics, Northeastern University, Boston, Massachusetts 02115, United States; Center for Theoretical Biological Physics, Northeastern University, Boston, Massachusetts 02115, United States; orcid.org/0000-0001-7104-2265; Email: p.whitford@northeastern.edu

Authors

Ailun Wang — Department of Chemistry, Boston College, Chestnut Hill, Massachusetts 02467, United States; Center for Theoretical Biological Physics, Northeastern University, Boston, Massachusetts 02115, United States; ○ orcid.org/ 0000-0002-4214-2352

Mariana Levi — Department of Physics, Northeastern University, Boston, Massachusetts 02115, United States

Complete contact information is available at: https://pubs.acs.org/10.1021/jacs.2c04082

Notes

The authors declare no competing financial interest.

ACKNOWLEDGMENTS

PCW was supported by NSF Grant MCB-1915843. Work at the Center for Theoretical Biological Physics was also supported by the NSF (Grant PHY-2019745). We acknowledge generous support provided the Northeastern University Research Computing staff, the Discovery Cluster and the C3DDB cluster. We would like to thank AMD for the donation of critical hardware and support resources from its HPC Fund that made this work possible. We thank Yang Wang for comments and proofreading the manuscript.

REFERENCES

- (1) Pyle, A. M. Metal ions in the structure and function of RNA. *J. Biol. Inorg. Chem.* **2002**, *7*, 679–690.
- (2) Woodson, S. A. Metal ions and RNA folding: a highly charged topic with a dynamic future. *Curr. Opin. Chem. Biol.* **2005**, *9*, 104–109.
- (3) Draper, D. E. A guide to ions and RNA structure. RNA **2004**, *10*, 335–343.
- (4) Draper, D. E.; Grilley, D.; Soto, A. M. Ions and RNA folding. *Annu. Rev. Biophys. Biomol. Struct.* **2005**, *34*, 221–243.
- (5) Schroeder, R.; Barta, A.; Semrad, K. Strategies for RNA folding and assembly. *Nat. Rev. Mol. Cell Biol.* **2004**, *5*, 908–919.
- (6) Wan, Y.; Qu, K.; Ouyang, Z.; Kertesz, M.; Li, J.; Tibshirani, R.; Makino, D. L.; Nutter, R. C.; Segal, E.; Chang, H. Y. Genome-wide measurement of RNA folding energies. *Mol. Cell* **2012**, *48*, 169–181.
- (7) Izatt, R. M.; Christensen, J. J.; Rytting, J. H. Sites and thermodynamic quantities associated with proton and metal ion interaction with ribonucleic acid, deoxyribonucleic acid, and their constituent bases, nucleosides, and nucleotides. *Chem. Rev.* 1971, 71, 439–481.
- (8) Shamsi, M. H.; Kraatz, H. B. Interactions of metal ions with DNA and some applications. *J. Inorg. Organomet. Polym. Mater.* **2013**, 23, 4–23.
- (9) Abeysirigunawardena, S. C.; Woodson, S. A. Differential effects of ribosomal proteins and Mg²⁺ ions on a conformational switch during 30S ribosome 5'-domain assembly. *RNA* **2015**, *21*, 1859–1865.
- (10) Kim, H. D.; Nienhaus, G. U.; Ha, T.; Orr, J. W.; Williamson, J. R.; Chu, S. Mg²⁺-dependent conformational change of RNA studied by fluorescence correlation and FRET on immobilized single molecules. *Proc. Natl. Acad. Sci. U.S.A.* **2002**, *99*, 4284–4289.
- (11) Klein, D. J.; Moore, P. B.; Steitz, T. A. The contribution of metal ions to the structural stability of the large ribosomal subunit. *RNA* **2004**, *10*, 1366–1379.
- (12) Gesteland, R. F. Unfolding of *Escherichia coli* ribosomes by removal of magnesium. *J. Mol. Biol.* **1966**, *18*, 356–371.
- (13) Kim, H. D.; Puglisi, J. D.; Chu, S. Fluctuations of transfer RNAs between classical and hybrid states. *Biophys. J.* **2007**, *93*, 3575–3582.
- (14) Holtkamp, W.; Cunha, C. E.; Peske, F.; Konevega, A. L.; Wintermeyer, W.; Rodnina, M. V. GTP hydrolysis by EF-G synchronizes tRNA movement on small and large ribosomal subunits. *EMBO J.* **2014**, 33, 1073–1085.

- (15) Wohlgemuth, I.; Pohl, C.; Rodnina, M. V. Optimization of speed and accuracy of decoding in translation. *EMBO J.* **2010**, *29*, 3701–3709
- (16) Johansson, M.; Zhang, J.; Ehrenberg, M. Genetic code translation displays a linear trade-off between efficiency and accuracy of tRNA selection. *Proc. Natl. Acad. Sci. U.S.A.* **2012**, *109*, 131–136.
- (17) Braunlin, W. H. NMR studies of cation-binding environments on nucleic acids. *Adv. Biophys. Chem.* **1995**, *5*, 89–140.
- (18) Reid, S. S.; Cowan, J. A. Biostructural Chemistry of Magnesium Ion: Characterization of the Weak Binding Sites on tRNAPhe(yeast). Implications for Conformational Change and Activity. *Biochemistry* 1990, 29, 6025–6032.
- (19) Cowan, J. A. Coordination chemistry of Mg²⁺ and 5S rRNA (*Escherichia coli*): Binding parameters, ligand symmetry, and implications for activity. *J. Am. Chem. Soc.* **1991**, *113*, 675–676.
- (20) Kowerko, D.; König, S. L.; Skilandat, M.; Kruschel, D.; Hadzic, M. C.; Cardo, L.; Sigel, R. K. Cation-induced kinetic heterogeneity of the intron-exon recognition in single group II introns. *Proc. Natl. Acad. Sci. U. S. A.* **2015**, *112*, 3403–3408.
- (21) Caminiti, R.; Licheri, G.; Piccaluga, G.; Pinna, G. X-ray diffraction study of MgCl₂ aqueous solutions. *J. Appl. Crystallogr.* **1979**, *12*, 34–38.
- (22) Weingärtner, H.; Müller, K. J.; Hertz, H. G.; Edge, A. V.; Mills, R. Unusual behavior of transport coefficients in aqueous solutions of zinc chloride at 25°C. *J. Phys. Chem.* **1984**, *88*, 2173–2178.
- (23) Bleuzen, A.; Pittet, P. A.; Helm, L.; Merbach, A. E. Water exchange on magnesium(II) in aqueous solution: A variable temperature and pressure ¹⁷O NMR study. *Magn. Reson. Chem.* **1997**, *35*, 765–773.
- (24) Cole, P. E.; Yang, S. K.; Crothers, D. M. Conformational changes of transfer ribonucleic acid. Equilibrium phase diagrams. *Biochemistry* **1972**, *11*, 4358–4368.
- (25) Urbanke, C.; Römer, R.; Maass, G. Tertiary structure of tRNA^{Phe} (Yeast): Kinetics and electrostatic repulsion. *Eur. J. Biochem.* **1975**, *55*, 439–444.
- (26) Denesyuk, N. A.; Thirumalai, D. How do metal ions direct ribozyme folding? *Nat. Chem.* **2015**, *7*, 793–801.
- (27) Hori, N.; Denesyuk, N. A.; Thirumalai, D. Shape changes and cooperativity in the folding of the central domain of the 16S ribosomal RNA. *Proc. Natl. Acad. Sci. U.S.A.* **2021**, *118*, No. e2020837118.
- (28) Fuoss, R. M.; Katchalsky, A.; Lifson, S. The potential of an infinite rod-like molecule and the distribution of the counter ions. *Proc. Natl. Acad. Sci. U.S.A.* **1951**, *37*, 579–589.
- (29) Honig, B.; Nicholls, A. Classical electrostatics in biology and chemistry. *Science* **1995**, *268*, 1144–1149.
- (30) Forsman, J. A simple correlation-corrected Poisson-Boltzmann theory. *J. Phys. Chem. B* **2004**, *108*, 9236–9245.
- (31) Manning, G. S. The molecular theory of polyelectrolyte solutions with applications to the electrostatic properties of polynucleotides. *Q. Rev. Biophys.* **1978**, *11*, 179–246.
- (32) Mohanty, U.; Ninham, B. W.; Oppenheim, I. Dressed polyions, counterion condensation, and adsorption excess in polyelectrolyte solutions. *Proc. Natl. Acad. Sci. U.S.A.* **1996**, 93, 4342–4344.
- (33) Manning, G. S.; Mohanty, U. Counterion condensation on ionic oligomers. *Phys. A: Stat. Mech. and its Appl.* **1997**, 247, 196–204.
- (34) Mohanty, U.; Spasic, A.; Kim, H. D.; Chu, S. Ion atmosphere of three-way junction nucleic acid. *J. Phys. Chem. B* **2005**, *109*, 21369—21374
- (35) Taubes, C. H.; Mohanty, U.; Chu, S. Ion atmosphere around nucleic acid. *J. Phys. Chem. B* **2005**, *109*, 21267–21272.
- (36) Spasic, A.; Mohanty, U. Counterion condensation in nucleic acid. *Adv. Chem. Phys.* **2008**, *139*, 139–176.
- (37) Hirata, F.; Rossky, P. J. An extended rism equation for molecular polar fluids. *Chem. Phys. Lett.* **1981**, *83*, 329–334.
- (38) Pettitt, B. M.; Rossky, P. J. Integral equation predictions of liquid state structure for waterlike intermolecular potentials. *J. Chem. Phys.* **1982**, *77*, 1451–1457.

- (39) Nguyen, H. T.; Hori, N.; Thirumalai, D. Theory and simulations for RNA folding in mixtures of monovalent and divalent cations. *Proc. Natl. Acad. Sci. U.S.A.* **2019**, *116*, 21022–21030.
- (40) Kjellander, R. Modified Debye-Hückel approximation with effective charges: An application of dressed ion theory for electrolyte solutions. *J. Phys. Chem.* **1995**, *99*, 10392–10407.
- (41) Frusawa, H.; Hayakawa, R. Generalizing the Debye-Hückel equation in terms of density functional integral. *Phys. Rev. E* **2000**, *61*, R6079—R6082.
- (42) Denesyuk, N. A.; Thirumalai, D. Coarse-grained model for predicting RNA folding thermodynamics. *J. Phys. Chem. B* **2013**, *117*, 4901–4911.
- (43) Schaefer, M.; Karplus, M. A comprehensive analytical treatment of continuum electrostatics. *J. Phys. Chem.* **1996**, *100*, 1578–1599.
- (44) Bashford, D.; Case, D. A. Generalized born models of macromolecular solvation effects. *Annu. Rev. Phys. Chem.* **2000**, *51*, 129–152.
- (45) Murthy, C. S.; Bacquet, R. J.; Rossky, P. J. Ionic distributions near polyelectrolytes. A comparison of theoretical approaches. *J. Phys. Chem.* **1985**, *89*, 701–710.
- (46) Netz, R. R.; Orland, H. Beyond Poisson-Boltzmann: Fluctuation effects and correlation functions. *Eur. Phys. J. E* **2000**, *1*, 203–214.
- (47) Attard, P. Electrolytes and the electric double layer. *Adv. Chem. Phys.* **1996**, 92, 1–159.
- (48) Shi, Y. Z.; Wang, F. H.; Wu, Y. Y.; Tan, Z. J. A coarse-grained model with implicit salt for RNAs: Predicting 3D structure, stability and salt effect. *J. Chem. Phys.* **2014**, *141*, 105102.
- (49) Marcovitz, A.; Levy, Y. Frustration in protein-DNA binding influences conformational switching and target search kinetics. *Proc. Natl. Acad. Sci. U. S. A.* **2011**, *108*, 17957–17962.
- (50) Givaty, O.; Levy, Y. Protein sliding along DNA: Dynamics and structural characterization. *J. Mol. Biol.* **2009**, 385, 1087–1097.
- (51) Wong, G. C.; Pollack, L. Electrostatics of strongly charged biological polymers: Ion-mediated interactions and self-organization in nucleic acids and proteins. *Annu. Rev. Phys. Chem.* **2010**, *61*, 171–189.
- (52) Savelyev, A.; Papoian, G. A. Molecular renormalization group coarse-graining of electrolyte solutions: Application to aqueous NaCl and KCl. *J. Phys. Chem. B* **2009**, *113*, 7785–7793.
- (53) Savelyev, A.; Papoian, G. A. Chemically accurate coarse graining of double-stranded DNA. *Proc. Natl. Acad. Sci. U.S.A.* **2010**, *107*, 20340–20345.
- (54) Denesyuk, N. A.; Hori, N.; Thirumalai, D. Molecular simulations of ion effects on the thermodynamics of RNA folding. *J. Phys. Chem. B* **2018**, *122*, 11860–11867.
- (55) Åqvist, J. Ion-water interaction potentials derived from free energy perturbation simulations. J. Phys. Chem. 1990, 94, 8021–8024.
- (56) Joung, I. S.; Cheatham, T. E., III Determination of alkali and halide monovalent ion parameters for use in explicitly solvated biomolecular simulations. *J. Phys. Chem. B* **2008**, *112*, 9020–9041.
- (57) Chen, A. A.; Pappu, R. V. Parameters of monovalent ions in the AMBER-99 forcefield: Assessment of inaccuracies and proposed improvements. *J. Phys. Chem. B* **2007**, *111*, 11884–11887.
- (58) Kirmizialtin, S.; Pabit, S. A.; Meisburger, S. P.; Pollack, L.; Elber, R. RNA and its ionic cloud: Solution scattering experiments and atomically detailed simulations. *Biophys. J.* **2012**, *102*, 819–828.
- (59) Chen, A. A.; García, A. E. High-resolution reversible folding of hyperstable RNA tetraloops using molecular dynamics simulations. *Proc. Natl. Acad. Sci. U.S.A.* **2013**, *110*, 16820–16825.
- (60) Miner, J. C.; García, A. E. Concentration-dependent and configuration-dependent interactions of monovalent ions with an RNA tetraloop. *J. Chem. Phys.* **2018**, *148*, 222837.
- (61) Srivastava, A.; Timsina, R.; Heo, S.; Dewage, S. W.; Kirmizialtin, S.; Qiu, X. Structure-guided DNA–DNA attraction mediated by divalent cations. *Nucleic Acid Res.* **2020**, *48*, 7018–7026.
- (62) Arenz, S.; Bock, L. V.; Graf, M.; Innis, C. A.; Beckmann, R.; Grubmüller, H.; Vaiana, A. C.; Wilson, D. N. A combined cryo-EM and molecular dynamics approach reveals the mechanism of ErmBL-mediated translation arrest. *Nat. Commun.* **2016**, *7*, 12026.

- (63) Whitford, P. C.; Noel, J. K.; Gosavi, S.; Schug, A.; Sanbonmatsu, K. Y.; Onuchic, J. N. An all-atom structure-based potential for proteins: Bridging minimal models with all-atom empirical forcefields. *Prot. Struct. Funct. Bioinfo.* **2009**, *75*, 430–441.
- (64) Noel, J. K.; Levi, M.; Raghunathan, M.; Lammert, H.; Hayes, R. L.; Onuchic, J. N.; Whitford, P. C. SMOG 2: A versatile software package for generating structure-based models. *PLoS Comput. Biol.* **2016**, *12*, No. e1004794.
- (65) Lindorff-Larsen, K.; Piana, S.; Palmo, K.; Maragakis, P.; Klepeis, J. L.; Dror, R. O.; Shaw, D. E. Improved side-chain torsion potentials for the Amber ff99SB protein force field. *Prot. Struct. Funct. Bioinfo.* **2010**, 78, 1950–1958.
- (66) Whitford, P. C.; Jiang, W.; Serwer, P. Simulations of phage T7 capsid expansion reveal the role of molecular sterics on dynamics. *Viruses* **2020**, *12*, 1273.
- (67) Noel, J. K.; Whitford, P. C.; Onuchic, J. N. The shadow map: A general contact definition for capturing the dynamics of biomolecular folding and function. *J. Phys. Chem. B* **2012**, *116*, 8692–8702.
- (68) Zhang, C.; Raugei, S.; Eisenberg, B.; Carloni, P. Molecular dynamics in physiological solutions: Force fields, alkali metal ions, and ionic strength. *J. Chem. Theory Comput.* **2010**, *6*, 2167–2175.
- (69) Timasheff, S. N. Water as ligand: Preferential binding and exclusion of denaturants in protein unfolding. *Biochem* **1992**, *31*, 9857–9864.
- (70) Eisenberg, H. Biological Macromolecules and Polyelectrolytes in Solution; Clarendon Press, 1976.
- (71) Rice, S. A.; Nagasawa, M. Polyelectrolyte Solutions; Academic Press: New York, 1961.
- (72) Grilley, D.; Misra, V.; Caliskan, G.; Draper, D. E. Importance of partially unfolded conformations for Mg²⁺-induced folding of RNA tertiary structure: Structural models and free energies of Mg²⁺ interactions. *Biochem* **2007**, *46*, 10266–10278.
- (73) Leipply, D.; Draper, D. E. Effects of Mg²⁺ on the free energy landscape for folding a purine riboswitch RNA. *Biochem* **2011**, *50*, 2790–2799.
- (74) Serganov, A.; Yuan, Y.-R.; Pikovskaya, O.; Polonskaia, A.; Malinina, L.; Phan, A. T.; Hobartner, C.; Micura, R.; Breaker, R. R.; Patel, D. J. Structural basis for discriminative regulation of gene expression by adenine- and guanine-sensing mRNAs. *Chem. Biol.* **2004**, *11*, 1729–1741.
- (75) Noeske, J.; Schwalbe, H.; Wöhnert, J. Metal-ion binding and metal-ion induced folding of the adenine-sensing riboswitch aptamer domain. *Nucleic Acids Res.* **2007**, *35*, 5262–5273.
- (76) Conn, G. L.; Gittis, A. G.; Lattman, E. E.; Misra, V. K.; Draper, D. E. A compact RNA tertiary structure contains a buried backbone—K⁺ complex. *J. Mol. Biol.* **2002**, *318*, 963–973.
- (77) Hayes, R. L.; Noel, J. K.; Mohanty, U.; Whitford, P. C.; Hennelly, S. P.; Onuchic, J. N.; Sanbonmatsu, K. Y. Magnesium fluctuations modulate RNA dynamics in the SAM-I riboswitch. *J. Am. Chem. Soc.* **2012**, *134*, 12043–12053.
- (78) Hayes, R. L.; Noel, J. K.; Whitford, P. C.; Mohanty, U.; Sanbonmatsu, K. Y.; Onuchic, J. N. Reduced model captures Mg²⁺-RNA interaction free energy of riboswitches. *Biophys. J.* **2014**, *106*, 1508–1519.
- (79) Misra, V. K.; Draper, D. E. A thermodynamic framework for Mg²⁺ binding to RNA. *Proc. Natl. Acad. Sci. U.S.A.* **2001**, 98, 12456–12461.
- (80) Xi, K.; Wang, F. H.; Xiong, G.; Zhang, Z. L.; Tan, Z. J. Competitive binding of Mg²⁺ and Na⁺ ions to nucleic acids: from helices to tertiary structures. *Biophys. J.* **2018**, *114*, 1776–1790.
- (81) Lammert, H.; Wang, A.; Mohanty, U.; Onuchic, J. N. RNA as a complex polymer with coupled dynamics of ions and water in the outer solvation sphere. *J. Phys. Chem. B* **2018**, *122*, 11218–11227.
- (82) Rodnina, M. V.; Wintermeyer, W. Fidelity of aminoacyl-tRNA selection on the ribosome: kinetic and structural mechanisms. *Annu. Rev. Biochem.* **2001**, *70*, 415–435.
- (83) Whitford, P. C.; Geggier, P.; Altman, R. B.; Blanchard, S. C.; Onuchic, J. N.; Sanbonmatsu, K. Y. Accommodation of aminoacyltRNA into the ribosome involves reversible excursions along multiple pathways. *RNA* **2010**, *16*, 1196–1204.

- (84) Noel, J. K.; Chahine, J.; Leite, V. B. P.; Whitford, P. C. Capturing Transition Paths and Transition States for Conformational Rearrangements in the Ribosome. Biophys. J. 2014, 107, 2881-2890.
- (85) Yang, H.; Noel, J. K.; Whitford, P. C. Anisotropic Fluctuations in the Ribosome Determine tRNA Kinetics. J. Phys. Chem. B 2017, 121, 10593-10601.
- (86) Yang, H.; Perrier, J.; Whitford, P. C. Disorder guides domain rearrangement in elongation factor Tu. Prot. Struct. Funct. Bioinfo. 2018, 86, 1037-1046.
- (87) Noel, J. K.; Whitford, P. C. How EF-Tu can contribute to efficient proofreading of aa-tRNA by the ribosome. Nat. Commun. 2016, 7, 13314.
- (88) Whitford, P.; Onuchic, J.; Sanbonmatsu, K. Connecting Energy Landscapes with Experimental Rates for Aminoacyl-tRNA Accommodation in the Ribosome. J. Am. Chem. Soc. 2010, 132, 13170–13171.
- (89) Yang, H.; Bandarkar, P.; Horne, R.; Leite, V. B.; Chahine, J.; Whitford, P. C. Diffusion of tRNA inside the ribosome is positiondependent. J. Chem. Phys. 2019, 151, 085102.
- (90) Sanbonmatsu, K. Y.; Joseph, S.; Tung, C.-S. Simulating movement of tRNA into the ribosome during decoding. Proc. Natl. Acad. Sci. U.S.A. 2005, 102, 15854-15859.
- (91) Rozov, A.; Khusainov, I.; El Omari, K.; Duman, R.; Mykhaylyk, V.; Yusupov, M.; Westhof, E.; Wagner, A.; Yusupova, G. Importance of potassium ions for ribosome structure and function revealed by longwavelength X-ray diffraction. Nat. Commun. 2019, 10, 1-12.
- (92) Johansson, M.; Lovmar, M.; Ehrenberg, M. Rate and accuracy of bacterial protein synthesis revisited. Curr. Opin. Microbio. 2008, 11, 141 - 147.
- (93) Conn, G. L.; Draper, D. E.; Lattman, E. E.; Gittis, A. G. Crystal structure of a conserved ribosomal protein-RNA complex. Science **1999**, 284, 1171-1174.
- (94) Agrawal, R. K.; Linde, J.; Sengupta, J.; Nierhaus, K. H.; Frank, J. Localization of L11 protein on the ribosome and elucidation of its involvement in EF-G-dependent translocation. J. Mol. Biol. 2001, 311, 777-787.
- (95) Gao, H.; Sengupta, J.; Valle, M.; Korostelev, A.; Eswar, N.; Stagg, S. M.; Van Roey, P.; Agrawal, R. K.; Harvey, S. C.; Sali, A.; Chapman, M. S.; Frank, J. Study of the structural dynamics of the E. coli 70S ribosome using real-space refinement. Cell 2003, 113, 789-801.
- (96) Valle, M.; Zavialov, A.; Li, W.; Stagg, S. M.; Sengupta, J.; Nielsen, R. C.; Nissen, P.; Harvey, S. C.; Ehrenberg, M.; Frank, J. Incorporation of aminoacyl-tRNA into the ribosome as seen by cryo-electron microscopy. Nat. Struct. Biol. 2003, 10, 899-906.
- (97) Seo, H.-S.; Abedin, S.; Kamp, D.; Wilson, D. N.; Nierhaus, K. H.; Cooperman, B. S. EF-G-dependent GTPase on the ribosome. Conformational change and fusidic acid inhibition. Biochem 2006, 45, 2504-2514.
- (98) Rodnina, M. V.; Savelsbergh, A.; Matassova, N. B.; Katunin, V. I.; Semenkov, Y. P.; Wintermeyer, W. Thiostrepton inhibits the turnover but not the GTPase of elongation factor G on the ribosome. Proc. Natl. Acad. Sci. U.S.A. 1999, 96, 9586-9590.
- (99) Hayes, R. L.; Noel, J. K.; Mandic, A.; Whitford, P. C.; Sanbonmatsu, K. Y.; Mohanty, U.; Onuchic, J. N. Generalized Manning condensation model captures the RNA ion atmosphere. Phys. Rev. Lett. 2015, 114, 258105,
- (100) Hyeon, C.; Thirumalai, D. Capturing the essence of folding and functions of biomolecules using coarse-grained models. Nat. Commun. 2011, 2, 487.
- (101) Oliveira, A. B.; Contessoto, V. G.; Hassan, A.; Byju, S.; Wang, A.; Wang, Y.; Dodero-Rojas, E.; Mohanty, U.; Noel, J. K.; Onuchic, J. N.; Whitford, P. C. SMOG 2 and OpenSMOG: Expanding the limiting of structure-based models. Protein Sci. 2022, 31, 158-172.
- (102) Nguyen, K.; Yang, H.; Whitford, P. C. How the ribosomal A-site finger can lead to tRNA species-dependent dynamics. J. Phys. Chem. B 2017, 121, 2767-2775.
- (103) Levi, M.; Walak, K.; Wang, A.; Mohanty, U.; Whitford, P. C. A steric gate controls hybrid-state formation of tRNA on the ribosome. *Nat. Commun.* **2020**, 11, 1–12.

- (104) Trobro, S.; Aqvist, J. Role of ribosomal protein L27 in peptidyl transfer. Biochemistry 2008, 47, 4898-4906.
- (105) Vaiana, A. C.; Sanbonmatsu, K. Y. Stochastic gating and drugribosome interactions. J. Mol. Biol. 2009, 386, 648-661.
- (106) Trabuco, L. G.; Schreiner, E.; Eargle, J.; Cornish, P.; Ha, T.; Luthey-Schulten, Z.; Schulten, K. The role of L1 stalk-tRNA interaction in the ribosome elongation cycle. J. Mol. Biol. 2010, 402, 741-760.
- (107) Bock, L. V.; Blau, C.; Schröder, G. F.; Davydov, I. I.; Fischer, N.; Stark, H.; Rodnina, M. V.; Vaiana, A. C.; Grubmüller, H. Energy barriers and driving forces in tRNA translocation through the ribosome. Nat. Struct. Mol. Biol. 2013, 20, 1390-1396.
- (108) Johansson, M.; Ieong, K. W.; Trobro, S.; Strazewski, P.; Åqvist, J.; Pavlov, M. Y.; Ehrenberg, M. pH-sensitivity of the ribosomal peptidyl transfer reaction dependent on the identity of the A-site aminoacyltRNA. Proc. Natl. Acad. Sci. U.S.A. 2011, 108, 79-84.
- (109) Bock, L. V.; Blau, C.; Vaiana, A. C.; Grubmüller, H. Dynamic contact network between ribosomal subunits enables rapid large-scale rotation during spontaneous translocation. Nucleic Acid Res. 2015, 43, 6747-6760.
- (110) Sethi, A.; Eargle, J.; Black, A. A.; Luthey-Schulten, Z. Dynamical networks in tRNA: protein complexes. Proc. Natl. Acad. Sci. U.S.A. 2009, 106, 6620-6625.
- (111) Eargle, J.; Black, A. A.; Sethi, A.; Trabuco, L. G.; Luthey-Schulten, Z. Dynamics of Recognition between tRNA and elongation factor Tu. J. Mol. Biol. 2008, 377, 1382-1405.
- (112) Trobro, S.; Åqvist, J. Mechanism of peptide bond synthesis on the ribosome. Proc. Natl. Acad. Sci. U.S.A. 2005, 102, 12395-12400.
- (113) Gindulyte, A.; Bashan, A.; Agmon, I.; Massa, L.; Yonath, A.; Karle, J. The transition state for formation of the peptide bond in the ribosome. Proc. Natl. Acad. Sci. U.S.A. 2006, 103, 13327-13332.
- (114) With the large dimensions of the simulated systems, the free volume (i.e., volume excluding the RNA) only differs from the total volume by less than 0.01%.
- (115) Γ_{2+} was estimated for alternate parameter values by weighting each simulated frame by $\exp(-\beta \Delta E)$, where ΔE is the change in system energy upon introduction of a modified parameter.
- (116) The reduced energy unit ϵ is equal to 2 $k_{\rm B}T$. For Mg²⁺-O interactions, B_1 was changed from -0.73 to -0.89. For Mg²⁺-N interactions, it was changed from -0.86 to -1.02.
- (117) Twenty-one coordinates of Mg²⁺ ions were reported in the two asymmetric assemblies of the 58-mer (chain C and chain D in PDB 1HC8). Alignment of the monomers reveals 13 distinct binding positions, where 8 are occupied in both RNA molecules.